Semiclassical calculation of the vibrational echo

W. G. Noid, Gregory S. Ezra, and Roger F. Loring
Department of Chemistry and Chemical Biology, Baker Laboratory, Cornell University, Ithaca, New York 14853

The infrared echo measurement probes the time scales of the molecular motions that couple to a vibrational transition. Computation of the echo observable within rigorous quantum mechanics is problematic for systems with many degrees of freedom, motivating the development of semiclassical approximations to the nonlinear optical response. We present a semiclassical approximation to the echo observable, based on the Herman–Kluk propagator. This calculation requires averaging over a quantity generated by two pairs of classical trajectories and associated stability matrices, connected by a pair of phase-space jumps. Quantum, classical, and semiclassical echo calculations are compared for a thermal ensemble of noninteracting anharmonic oscillators. The semiclassical approach uses input from classical mechanics to reproduce the significant features of a complete, quantum mechanical calculation of the nonlinear response. © *2004 American Institute of Physics.* [DOI: 10.1063/1.1633550]

I. INTRODUCTION

In principle, the absorption line shape of a vibrational transition reflects the dynamics of nuclear degrees of freedom that interact with the transition. In practice, the spectral line shape may be dominated by slow dynamics, obscuring its full information content. Coherent multiple-pulse infrared measurements, analogous to pulse sequences of multidimensional NMR,[1] can sort spectral line broadening dynamics according to time scale, thereby probing nuclear dynamics in the ground electronic state.[2–8] Such measurements, including the two-pulse and three-pulse vibrational echo experiments,[5,9–16] have been successfully applied to liquid state and biomolecular systems.

The assignment of the temporal decays observed in coherent multiple-pulse infrared spectroscopy to specific molecular motions requires the computation of the observable for a microscopic, mechanical model. The challenges posed by large-scale time-dependent quantum mechanical calculations motivate the development of classical[17–26] and semiclassical[27–29] approaches to the observables of nonlinear spectroscopy. We have reported a semiclassical formalism[29] for the general nth-order optical response function $R^{(n)}$ that is based on the Herman–Kluk approximation[30–34] to the quantum mechanical propagator. Within this approach, $R^{(n)}$ is expressed as the average of a quantity that is computed from n pairs of classical trajectories with associated stability matrices, interrupted by $n-1$ phase space jumps. The trajectory pairs approximate quantum interference effects,[35–40] and the phase-space jumps represent the effects of the radiation-matter interaction. Calculations in the simplest case of linear response, $n=1$, for a thermal ensemble of anharmonic oscillators demonstrated that the method provides quantitative agreement with quantum mechanics for that case.[29] The linear response calculation involves computing interference effects from a single pair of classical trajectories without phase space jumps, and while its demonstrated accuracy is sugges-

tive, the full validation of the semiclassical method requires calculation of a nonlinear observable.

To lowest order in perturbation theory in the radiation-matter interaction, evaluating the observable in a two-pulse or three-pulse vibrational echo measurement requires calculation of the third-order response function $R^{(3)}(t_3,t_2,t_1)$.[41] We present here semiclassical calculations of $R^{(3)}(t_3,0,t_1)$, which is relevant to the two-pulse echo observable in the limit of impulsive excitation. This quantity is computed with the approach of Ref. 29 for a thermal ensemble of noninteracting Morse oscillators. The formalism[29] is reviewed in Sec. II, and general numerical strategies are discussed there. The model is also described in Sec. II, and the particular numerical procedures applied to this model are detailed. Calculations are presented in Sec. III, and conclusions drawn from these results are summarized in Sec. IV.

II. SEMICLASSICAL VIBRATIONAL ECHOES

Expansion of the classical mechanical electric polarization to third order in the electric field amplitude $E(t)$ defines the third-order optical response function,[41] $R^{(3)}(t_3,t_2,t_1)$, according to

$$P^{(3)}(t) = \int_0^\infty dt_3 \int_0^\infty dt_2 \int_0^\infty dt_1 R^{(3)}(t_3,t_2,t_1)$$
$$\times E(t-t_3)E(t-t_2-t_3)E(t-t_1-t_2-t_3), \quad (1)$$

in which t_1, t_2, and t_3 are elapsed times between successive radiation-matter interactions. The signal in a third-order measurement with homodyne detection, for an optically thin sample, may be related to the square of the appropriately phase-matched component[41] of $P^{(3)}$. The material system is taken to have F degrees of freedom, one of which is coupled to the radiation with an electric dipole interaction. The dipole is taken to be linear in this "active" coordinate $\hat{x}$, so that the response function can be expressed in terms of three nested commutators[41] involving $\hat{x}$ and the initial density operator $\hat{\rho}$

$$R^{(3)}(t_3,t_2,t_1)=\left(\frac{i}{\hbar}\right)^3 \mathrm{Tr}(\hat{x}\hat{K}(t_3)[\hat{x},\hat{K}(t_2)[\hat{x},\hat{K}(t_1)$$

$$\times[\hat{x},\hat{\rho}]\hat{K}^\dagger(t_1)]\hat{K}^\dagger(t_2)]\hat{K}^\dagger(t_3)), \qquad (2)$$

with $\hat{K}(t)\equiv\exp(-i\hat{H}t/\hbar)$ the propagator for a system with Hamiltonian $\hat{H}$. The proportionality constant between the coordinate and electric dipole operators has been suppressed.

Our approximation to $R^{(3)}$ is based on the Herman–Kluk (HK) semiclassical approximation[30–34] to the quantum propagator,

$$\hat{K}_{HK}(t)=(2\pi\hbar)^{-F}\int d\mathbf{z}\,|\mathbf{z}(t)\rangle G(\mathbf{z},t)\langle\mathbf{z}|, \qquad (3)$$

with

$$G(\mathbf{z},t)=C(\mathbf{z},t)\exp[iS(\mathbf{z},t)/\hbar], \qquad (4)$$

$$C(\mathbf{z},t)=\sqrt{\det\frac{1}{2}\left(\mathbf{M}_{qq}(\mathbf{z},t)+\mathbf{M}_{pp}(\mathbf{z},t)-i\hbar\gamma\mathbf{M}_{qp}(\mathbf{z},t)+\frac{i}{\hbar\gamma}\mathbf{M}_{pq}(\mathbf{z},t)\right)}. \qquad (5)$$

In the propagator of Eq. (3), $\mathbf{z}$ denotes a point in $2F$-dimensional phase space, $\mathbf{z}(t)$ represents the phase space point resulting from propagation of $\mathbf{z}$ for time t, and $|\mathbf{z}\rangle$ is the coherent state with coordinate-space wave function,

$$\langle\mathbf{r}|\mathbf{z}\rangle=\left(\frac{\gamma}{\pi}\right)^{F/4}\exp\left(-\frac{\gamma}{2}(\mathbf{r}-\mathbf{q})^2+\frac{i}{\hbar}\mathbf{p}\cdot(\mathbf{r}-\mathbf{q})\right). \qquad (6)$$

The spatial width parameter characterizing the coherent state is denoted γ, and $\mathbf{p}$ and $\mathbf{q}$ are the F-dimensional momenta and coordinates associated with that state. The classical action (Hamilton's principal function) is denoted $S(\mathbf{z},t)$ in Eq. (4). The complex-valued prefactor of the HK propagator, $C(\mathbf{z},t)$, is expressed in terms of stability matrices in Eq. (5). These are F-dimensional matrices, with elements given by, for example,

$$[\mathbf{M}_{qp}(\mathbf{z},t)]_{\alpha\beta}\equiv\left(\frac{\partial q_\alpha(t)}{\partial p_\beta(0)}\right)_{\{p_\nu(0)\}_{\nu\neq\beta}\{q_\nu(0)\}}, \qquad (7)$$

with α, β, and ν labeling degrees of freedom, and $\mathbf{z}\equiv(\mathbf{q}(0),\mathbf{p}(0))$. The active degree of freedom will be labeled $\alpha=0$.

Substitution of the propagator in Eq. (3) into Eq. (2) yields the $n=3$ case of the semiclassical nth-order response function presented in Eq. (14) of Ref. 29,

$$R^{(3)}(t_3,t_2,t_1)=\hbar^{-2}\int\frac{d\mathbf{z}_1}{(2\pi\hbar)^F}\int\frac{d\mathbf{z}_2}{(2\pi\hbar)^F}\cdots\int\frac{d\mathbf{z}_6}{(2\pi\hbar)^F}G(\mathbf{z}_1,t_1)G^*(\mathbf{z}_2,t_1)$$

$$\times G(\mathbf{z}_3,t_2)G^*(\mathbf{z}_4,t_2)G(\mathbf{z}_5,t_3)G^*(\mathbf{z}_6,t_3)\langle\mathbf{z}_6(t_3)|\mathbf{z}_5(t_3)\rangle\mathcal{X}(\mathbf{z}_6(t_3),\mathbf{z}_5(t_3))\langle\mathbf{z}_4(t_2)|\mathbf{z}_6\rangle$$

$$\times\langle\mathbf{z}_5|\mathbf{z}_3(t_2)\rangle[\mathcal{X}(\mathbf{z}_5,\mathbf{z}_3(t_2))-\mathcal{X}^*(\mathbf{z}_6,\mathbf{z}_4(t_2))]\langle\mathbf{z}_2(t_1)|\mathbf{z}_4\rangle\langle\mathbf{z}_3|\mathbf{z}_1(t_1)\rangle$$

$$\times[\mathcal{X}(\mathbf{z}_3,\mathbf{z}_1(t_1))-\mathcal{X}^*(\mathbf{z}_4,\mathbf{z}_2(t_1))]\langle\mathbf{z}_1|\mathbf{z}_2\rangle\frac{\partial}{\partial\bar{p}_{12}}\left(\frac{\langle\mathbf{z}_1|\hat{\rho}|\mathbf{z}_2\rangle}{\langle\mathbf{z}_1|\mathbf{z}_2\rangle}\right), \qquad (8)$$

with

$$\mathcal{X}(\mathbf{z}_j,\mathbf{z}_k)\equiv\frac{\langle\mathbf{z}_j|\hat{x}|\mathbf{z}_k\rangle}{\langle\mathbf{z}_j|\mathbf{z}_k\rangle}=\bar{q}_{jk}-i\frac{\Delta p_{jk}}{2\gamma\hbar}, \qquad (9)$$

$$\langle\mathbf{z}_j|\mathbf{z}_k\rangle=\exp\left(-\frac{\gamma(\Delta\mathbf{q}_{jk})^2}{4}-\frac{(\Delta\mathbf{p}_{jk})^2}{4\hbar^2\gamma}+\frac{i}{\hbar}\bar{\mathbf{p}}_{jk}\cdot\Delta\mathbf{q}_{jk}\right), \qquad (10)$$

$$\Delta\mathbf{x}_{jk}\equiv\mathbf{x}_j-\mathbf{x}_k;\quad\bar{\mathbf{x}}_{jk}\equiv(\mathbf{x}_j+\mathbf{x}_k)/2, \qquad (11)$$

$$\Delta x_{jk}=(\mathbf{x}_j)_0-(\mathbf{x}_k)_0;\quad\bar{x}_{jk}=[(\mathbf{x}_j)_0+(\mathbf{x}_k)_0]/2. \qquad (12)$$

In Eqs. (11) and (12), $\mathbf{x}$ denotes either coordinate or momentum.

The signal in a two-pulse vibrational echo measurement in the limit of impulsive excitation, in which nuclear dynamics have time scales long compared to laser pulse durations, can be calculated from the response function with $t_2=0$.[41] Setting $t_2=0$ in Eq. (8) permits the integrations over the phase space points $\mathbf{z}_3$ and $\mathbf{z}_4$ to be performed exactly, using the completeness[42] of coherent states,

$$R^{(3)}(t_3,0,t_1)=\hbar^{-2}\int\frac{d\mathbf{z}_1}{(2\pi\hbar)^F}\int\frac{d\mathbf{z}_2}{(2\pi\hbar)^F}\int\frac{d\mathbf{z}_5}{(2\pi\hbar)^F}\int\frac{d\mathbf{z}_6}{(2\pi\hbar)^F}G(\mathbf{z}_1,t_1)G^*(\mathbf{z}_2,t_1)$$

$$\times G(\mathbf{z}_5,t_3)G^*(\mathbf{z}_6,t_3)\langle\mathbf{z}_6(t_3)|\mathbf{z}_5(t_3)\rangle\mathcal{X}(\mathbf{z}_6(t_3),\mathbf{z}_5(t_3))\langle\mathbf{z}_2(t_1)|\mathbf{z}_6\rangle\langle\mathbf{z}_5|\mathbf{z}_1(t_1)\rangle$$

$$\times\{[\mathcal{X}(\mathbf{z}_5,\mathbf{z}_1(t_1))-\mathcal{X}^*(\mathbf{z}_6,\mathbf{z}_2(t_1))]^2+\gamma^{-1}\}\langle\mathbf{z}_1|\mathbf{z}_2\rangle\frac{\partial}{\partial\bar{p}_{12}}\left(\frac{\langle\mathbf{z}_1|\hat{\rho}|\mathbf{z}_2\rangle}{\langle\mathbf{z}_1|\mathbf{z}_2\rangle}\right).\tag{13}$$

The expression in Eq. (13) follows from a single approximation: the HK semiclassical propagator in Eq. (3). Evaluation of $R^{(3)}$ in Eq. (13) requires the density matrix in the coherent states representation. In the numerical calculations presented below, we treat the density matrix within the high-temperature approximation[32] discussed in Ref. 29,

$$(2\pi\hbar)^{-F}\frac{\langle\mathbf{z}_1|\hat{\rho}|\mathbf{z}_2\rangle}{\langle\mathbf{z}_1|\mathbf{z}_2\rangle}\to f_{cl}(\bar{\mathbf{z}}_{12}),\tag{14}$$

with the classical mechanical phase space distribution denoted f_{cl}. This approximation was shown to work well even at relatively low temperature for a semiclassical calculation of the linear response function.[29]

For a system of F degrees of freedom, the third-order response function is related in Eq. (13) to an $8F$-dimensional integral. Calculating the integrand in Eq. (13) for each choice of the times t_1 and t_3 requires computing two classical trajectories of duration t_1 originating at $\mathbf{z}_1$ and $\mathbf{z}_2$ and two trajectories of duration t_3 originating at $\mathbf{z}_5$ and $\mathbf{z}_6$. The initial conditions for the second pair of trajectories $\mathbf{z}_5$ and $\mathbf{z}_6$ are constrained to be close in phase space to the concluding phase-space points of the first pair of trajectories $\mathbf{z}_1(t_1)$ and $\mathbf{z}_2(t_1)$ by the coherent-state overlap factors $\langle\mathbf{z}_2(t_1)|\mathbf{z}_6\rangle$ $\times\langle\mathbf{z}_5|\mathbf{z}_1(t_1)\rangle$, whose form is given in Eq. (10). Performing the integration in Eq. (13) presents difficulties that also arise in the computation of a variety of dynamical properties with semiclassical propagators.[32,36–40] Though the integral is real-valued and finite, the integrand is complex-valued and divergent in time. This temporal divergence arises from the growth with time of the HK prefactors, $C(\mathbf{z},t)$ in Eq. (5), contained within $G(\mathbf{z},t)$ in Eq. (13), each of which diverges as the square root of time for the integrable model of the following section, and exponentially in the more general case of chaotic dynamics. Complex-valued divergent contributions to the integral of varying phase interfere to cancel the divergences and to approximate the oscillations characterizing quantum dynamics. An unbiased Monte Carlo evaluation is inappropriate for such an integral, and choice of an importance sampling procedure is a critical aspect of the calculation.

In the following section, we calculate the nonlinear response function for an ensemble of noninteracting one-dimensional anharmonic oscillators, $F=1$, by applying the "phase distribution" strategy proposed by Sun and Miller[43] to evaluate semiclassical approximations to correlation functions. In this procedure, the absolute magnitude of the complex-valued integrand is used as an unnormalized sampling distribution in a Metropolis Monte Carlo integration.

We write the complex-valued integrand in Eqs. (13) and (14) in terms of its absolute value J and phase Φ,

$$R^{(3)}(t_3,0,t_1)=\int d\mathbf{z}_1\int d\mathbf{z}_2\int d\mathbf{z}_5\int d\mathbf{z}_6$$

$$\times J(\mathbf{z}_1,\mathbf{z}_2,\mathbf{z}_5,\mathbf{z}_6;t_1,t_3)$$

$$\times\exp[i\Phi(\mathbf{z}_1,\mathbf{z}_2,\mathbf{z}_5,\mathbf{z}_6;t_1,t_3)],\tag{15}$$

$$J=\frac{\beta}{8\pi^3 m\hbar^5}|C(\mathbf{z}_1,t_1)C^*(\mathbf{z}_2,t_1)C(\mathbf{z}_5,t_3)C^*(\mathbf{z}_6,t_3)$$

$$\times\langle\mathbf{z}_6(t_3)|\mathbf{z}_5(t_3)\rangle\mathcal{X}(\mathbf{z}_6(t_3),\mathbf{z}_5(t_3))\langle\mathbf{z}_2(t_1)|\mathbf{z}_6\rangle$$

$$\times\langle\mathbf{z}_5|\mathbf{z}_1(t_1)\rangle\{[\mathcal{X}(\mathbf{z}_5,\mathbf{z}_1(t_1))-\mathcal{X}^*(\mathbf{z}_6,\mathbf{z}_2(t_1))]^2+\gamma^{-1}\}$$

$$\times\langle\mathbf{z}_1|\mathbf{z}_2\rangle\bar{p}_{12}f_{cl}(\bar{\mathbf{z}}_{12})|.\tag{16}$$

Use of J as a sampling distribution requires its normalization, with the associated definition of a weight function $W(t_1,t_3)$,

$$W(t_1,t_3)=\int d\mathbf{z}_1\int d\mathbf{z}_2\int d\mathbf{z}_5\int d\mathbf{z}_6 J(\mathbf{z}_1,\mathbf{z}_2,\mathbf{z}_5,\mathbf{z}_6;t_1,t_3).\tag{17}$$

The response function is then expressed in terms of a normalized sampling distribution $P(\mathbf{z}_1,\mathbf{z}_2,\mathbf{z}_5,\mathbf{z}_6;t_1,t_3)$ $\equiv J(\mathbf{z}_1,\mathbf{z}_2,\mathbf{z}_5,\mathbf{z}_6;t_1,t_3)/W(t_1,t_3)$,

$$R^{(3)}(t_3,0,t_1)$$

$$=W(t_1,t_3)\int d\mathbf{z}_1\int d\mathbf{z}_2\int d\mathbf{z}_5\int d\mathbf{z}_6 P\exp[i\Phi].\tag{18}$$

Application of the Metropolis algorithm[44] produces

$$R^{(3)}(t_3,0,t_1)\approx\frac{W(t_1,t_3)}{N}\sum_s\exp[i\Phi(\mathbf{Z}_s)].\tag{19}$$

A set of values of $\{\mathbf{z}_1,\mathbf{z}_2,\mathbf{z}_5,\mathbf{z}_6\}$ is denoted $\mathbf{Z}_s$, with the index s labeling the N steps in a Metropolis random walk through $\mathbf{Z}$ space. According to the Metropolis procedure, the

point $\mathbf{Z}_{s+1}$ is included with unit probability if $J(\mathbf{Z}_{s+1}) > J(\mathbf{Z}_s)$ and with probability $J(\mathbf{Z}_{s+1})/J(\mathbf{Z}_s)$ otherwise. This sampling procedure has the advantage that the temporally divergent contributions to the integrand are included in the sampling function, so that the integral is expressed in Eq. (19) as a sum of complex-valued terms of unit absolute value.

Unlike the integrand in Eq. (15), the integrand in Eq. (17) is positive definite. Nevertheless, the integral required to compute W in Eq. (17) is itself a candidate for evaluation by a Monte Carlo method with importance sampling. One choice for an unnormalized sampling distribution for this integral is

$$J_0(\mathbf{z}_1,\mathbf{z}_2,\mathbf{z}_5,\mathbf{z}_6;t_1)=|\langle\mathbf{z}_2(t_1)|\mathbf{z}_6\rangle\langle\mathbf{z}_5|\mathbf{z}_1(t_1)\rangle$$
$$\times\langle\mathbf{z}_1|\mathbf{z}_2\rangle|f_{cl}(\overline{\mathbf{z}}_{12}). \quad (20)$$

This distribution emphasizes regions of the integration space with the following properties. The second set of phase-space points, $\mathbf{z}_5$ and $\mathbf{z}_6$, are "close" in the sense described above to the concluding phase-space points of the initial pair of trajectories, $\mathbf{z}_1(t_1)$ and $\mathbf{z}_2(t_1)$, $\mathbf{z}_1$ and $\mathbf{z}_2$ are close in this sense, and initial mean momenta and coordinates, $\overline{\mathbf{z}}_{12}$, are associated with large values of a Boltzmann distribution. This sampling distribution also has the advantage that it can be normalized analytically,

$$W_0 = \int d\mathbf{z}_1 \int d\mathbf{z}_2 \int d\mathbf{z}_5 \int d\mathbf{z}_6 J_0(\mathbf{z}_1,\mathbf{z}_2,\mathbf{z}_5,\mathbf{z}_6;t_1)$$
$$= (4\pi\hbar)^{3F}. \quad (21)$$

For the model treated in the following section, we have determined empirically that the integral in Eq. (17) may be more efficiently sampled using a multistep procedure described below, than by using the distribution in Eq. (20). Calculations of W from Eq. (17) using the unnormalized sampling distribution J_0 yield an answer that is noisier and that appears to converge towards a different result compared to a calculation with the same number of sampling points using the multistep method described below. As shown in the following section, $R^{(3)}$ calculated using W evaluated by the multistep procedure generally agrees with exact quantum mechanics. Using W sampled according to J_0 produces an $R^{(3)}$ result that is systematically too large. The less than optimal sampling provided by the distribution J_0 suggests the use of an alternative distribution that depends on the endpoints of the second pair of trajectories, $\mathbf{z}_5(t_3)$ and $\mathbf{z}_6(t_3)$. An analogy may be drawn to the simulation of rare events, where sampling procedures must emphasize trajectories starting in an "initial" or "reactant" state that eventually reach a region of configuration space representing a "final" or "product" state.[43,45]

A more efficient sampling procedure for the integral in Eq. (17) may be devised by identifying factors in the integrand J that are significant on different time scales. We write J in Eq. (16) in terms of a factor $\mathcal{C}$ that contains the temporally diverging HK prefactors, a factor X that contains coherent-state matrix elements of the coordinate operator, a factor $\mathcal{O}$ containing overlaps of coherent states, and f_{cl}, the classical phase space distribution,

$$J = \mathcal{C}X\mathcal{O}f_{cl}(\overline{\mathbf{z}}_{12}), \quad (22)$$

$$\mathcal{C} = \frac{\beta}{8\pi^3 m\hbar^5}|C(\mathbf{z}_1,t_1)C^*(\mathbf{z}_2,t_1)C(\mathbf{z}_5,t_3)C^*(\mathbf{z}_6,t_3)|, \quad (23)$$

$$X = |\mathcal{X}(\mathbf{z}_6(t_3),\mathbf{z}_5(t_3))\{[\mathcal{X}(\mathbf{z}_5,\mathbf{z}_1(t_1))-\mathcal{X}^*(\mathbf{z}_6,\mathbf{z}_2(t_1))]^2$$
$$+\gamma^{-1}\}\overline{p}_{12}|, \quad (24)$$

$$\mathcal{O} = |\langle\mathbf{z}_6(t_3)|\mathbf{z}_5(t_3)\rangle\langle\mathbf{z}_2(t_1)|\mathbf{z}_6\rangle\langle\mathbf{z}_5|\mathbf{z}_1(t_1)\rangle\langle\mathbf{z}_1|\mathbf{z}_2\rangle|. \quad (25)$$

For the Morse oscillator model described below, we have observed that for relatively small values of t_1 and t_3, J is dominated by the factor

$$J_1(\mathbf{z}_1,\mathbf{z}_2,\mathbf{z}_5,\mathbf{z}_6;t_1,t_3)=\mathcal{O}(\mathbf{z}_1,\mathbf{z}_2,\mathbf{z}_5,\mathbf{z}_6;t_1,t_3)f_{cl}(\overline{\mathbf{z}}_{12}). \quad (26)$$

The unnormalized sampling distribution J_1 differs from J_0 in Eq. (20) in the inclusion of the absolute value of an overlap factor for the final coherent states, $|\langle\mathbf{z}_6(t_3)|\mathbf{z}_5(t_3)\rangle|$, which constrains the endpoints of the second trajectory pair to be close in phase space. On the time scale of the energy-dependent period of the anharmonic oscillator, the factor X becomes significant. This factor is a quartic function of the averages and differences of positions and momenta of various trajectory pairs, and its value can span several orders of magnitude. It is necessary to assign correct statistical weights to sets of trajectories for which this factor is large. However, because the coordinates and momenta of the oscillator are bounded for a given energy, at long times J is dominated by $\mathcal{C}$ in Eq. (23), which increases without bound for increasing t_1 and t_3.

Because of the approximate separation of time scales associated with the different factors in J that are shown in Eq. (22), we adopt a procedure that treats these factors separately. The calculation of W in Eq. (17) is carried out as a series of nested integrations, such that contributions to J that are important at ever later time scales are successively incorporated at each stage. We begin by using the analytically normalizable sampling distribution J_0 in Eq. (20) to evaluate the integral of J_1 in Eq. (26),

$$W_1(t_1,t_3)$$
$$= \int d\mathbf{z}_1 \int d\mathbf{z}_2 \int d\mathbf{z}_5 \int d\mathbf{z}_6 J_1(\mathbf{z}_1,\mathbf{z}_2,\mathbf{z}_5,\mathbf{z}_6;t_1,t_3), \quad (27)$$
$$= W_0 \int d\mathbf{z}_1 \int d\mathbf{z}_2 \int d\mathbf{z}_5 \int d\mathbf{z}_6$$
$$\times P_0(\mathbf{z}_1,\mathbf{z}_2,\mathbf{z}_5,\mathbf{z}_6;t_1)|\langle\mathbf{z}_6(t_3)|\mathbf{z}_5(t_3)\rangle|. \quad (28)$$

The integral in Eq. (28) is evaluated by a Monte Carlo method with sampling distribution $P_0 \equiv J_0/W_0$,

$$P_0(\mathbf{z}_1,\mathbf{z}_2,\mathbf{z}_5,\mathbf{z}_6;t_1)$$
$$= (4\pi\hbar)^{-3F}\exp\left(-\frac{\gamma}{4}(\Delta q_{62t_1}^2+\Delta q_{51t_1}^2+\Delta q_{12}^2)\right)$$
$$\times\exp\left(-\frac{1}{4\gamma\hbar^2}(\Delta p_{62t_1}^2+\Delta p_{51t_1}^2+\Delta p_{12}^2)\right)f_{cl}(\overline{\mathbf{z}}_{12}), \quad (29)$$

$$\Delta \mathbf{z}_{jkt} \equiv \mathbf{z}_j - \mathbf{z}_k(t). \tag{30}$$

The distribution P_0 is expressed here in terms of the mean and difference variables of the initial conditions for the first pair of trajectories $\overline{\mathbf{z}}_{12}$ and $\Delta \mathbf{z}_{12}$ and in terms of difference variables connecting the endpoints of the first pair of trajectories to the initial conditions of the second trajectory pair $\Delta \mathbf{z}_{62t_1}$ and $\Delta \mathbf{z}_{51t_1}$. The distribution is Gaussian in all variables except the mean initial coordinate $\overline{\mathbf{q}}_{12}$. While the form of P_0 is independent of t_1, generating the value of the distribution for a given set of $\{\mathbf{z}_1, \mathbf{z}_2, \mathbf{z}_5, \mathbf{z}_6\}$ requires calculation of two trajectories of duration t_1. These trajectories determine $\mathbf{z}_1(t_1)$ and $\mathbf{z}_2(t_1)$, which, for given $\Delta \mathbf{z}_{62t_1}$ and $\Delta \mathbf{z}_{51t_1}$, specify the values of $\mathbf{z}_5$ and $\mathbf{z}_6$.

The weight function W_1 is required in the normalization of a sampling distribution J_2, which incorporates X in Eq. (24),

$$J_2(\mathbf{z}_1, \mathbf{z}_2, \mathbf{z}_5, \mathbf{z}_6; t_1, t_3)$$
$$= J_1(\mathbf{z}_1, \mathbf{z}_2, \mathbf{z}_5, \mathbf{z}_6; t_1, t_3) X(\mathbf{z}_1, \mathbf{z}_2, \mathbf{z}_5, \mathbf{z}_6; t_1, t_3), \tag{31}$$

$$W_2(t_1, t_3)$$
$$= \int d\mathbf{z}_1 \int d\mathbf{z}_2 \int d\mathbf{z}_5 \int d\mathbf{z}_6 J_2(\mathbf{z}_1, \mathbf{z}_2, \mathbf{z}_5, \mathbf{z}_6; t_1, t_3), \tag{32}$$

$$= W_1(t_1, t_3) \int d\mathbf{z}_1 \int d\mathbf{z}_2 \int d\mathbf{z}_5 \int d\mathbf{z}_6$$
$$\times P_1(\mathbf{z}_1, \mathbf{z}_2, \mathbf{z}_5, \mathbf{z}_6; t_1, t_3) X(\mathbf{z}_1, \mathbf{z}_2, \mathbf{z}_5, \mathbf{z}_6; t_1, t_3). \tag{33}$$

The normalization factor W_2 in Eq. (33) is evaluated by the Metropolis method with sampling distribution $P_1 \equiv J_1/W_1$. In each step of the Metropolis random walk, the quantities $\overline{\mathbf{z}}_{12}$, $\Delta \mathbf{z}_{12}$, $\Delta \mathbf{z}_{62t_1}$, and $\Delta \mathbf{z}_{51t_1}$ are varied. A final application of this procedure yields $W(t_1, t_3)$ in Eq. (17),

$$W(t_1, t_3) = W_2(t_1, t_3) \int d\mathbf{z}_1 \int d\mathbf{z}_2 \int d\mathbf{z}_5 \int d\mathbf{z}_6$$
$$\times P_2(\mathbf{z}_1, \mathbf{z}_2, \mathbf{z}_5, \mathbf{z}_6; t_1, t_3) \mathcal{C}. \tag{34}$$

This integral is computed with sampling distribution $P_2 \equiv J_2/W_2$. Our calculation of $R^{(3)}(t_3, 0, t_1)$ at fixed values of t_1 and t_3 thus requires four nested Monte Carlo integrations. The integral in Eq. (28) yields W_1, which is used to calculate W_2 in Eq. (33), which in turn is required to compute W in Eq. (34), which is then applied to evaluate $R^{(3)}$ in Eq. (18). This calculation is particularly numerically demanding, because the sampling distributions in each of these integrals are time dependent. Evaluation of the magnitude of the sampling distribution for a particular set of initial conditions $\mathbf{z}_1, \mathbf{z}_2, \mathbf{z}_5, \mathbf{z}_6$ requires computation of a pair of trajectories of duration t_1 in the case of P_0 in Eq. (28), and requires computation of an additional trajectory pair of duration t_3 in the cases of P_1 in Eq. (33) and P_2 in Eq. (34).

We apply this procedure in the following section to compute $R^{(3)}(t_3, 0, t_1)$ for a thermal ensemble of noninteracting Morse oscillators,[29] each with Hamiltonian

$$\hat{H} = \frac{\hat{p}^2}{2m} + D(1 - e^{-\alpha \hat{q}})^2. \tag{35}$$

The density matrix has the canonical form $\hat{\rho} = \exp(-\beta \hat{H})/ \mathrm{Tr}\{\exp(-\beta \hat{H})\}$. Calculations with the HK propagator require specifying a value for the coherent-states width parameter γ in Eq. (6). For the calculations presented here, γ was assigned a value close to that appropriate to a harmonic oscillator, $\gamma \approx \sqrt{m\omega/\hbar}$. Here, ω is the harmonic frequency of the Morse oscillator, given by

$$\omega = \alpha \sqrt{\frac{2D}{m}}. \tag{36}$$

In the linear-response calculations of Ref. 29, we explored the effects of varying the magnitude of γ, and demonstrated that accuracy and convergence are optimized[46] for values in this range. Time-dependent phase-space coordinates, stability matrices, and Hamilton's principal function were computed without numerical integration, using the analytical formulation of dynamics of the Morse oscillator in terms of action-angle variables.[29,47,48] The existence of an analytical solution for the Morse oscillator dynamics allows these quantities to be calculated at a given set of time variables, without computing their values over a range of earlier times. However, coarse-grained trajectories were computed to ensure the correct choice of branch in the complex square root involved in the HK prefactors in Eq. (5).

The integration in Eq. (28) was performed by a Monte Carlo procedure using the nearly Gaussian sampling distribution P_0 in Eq. (29). For each set of time values, 10^5 sets of four time-propagations sufficed to attain convergence. The integrations in Eqs. (33), (34), and (18) were performed by Metropolis Monte Carlo. Metropolis moves in the eight variables $\{\overline{\mathbf{z}}_{12}, \Delta \mathbf{z}_{12}, \Delta \mathbf{z}_{62t_1}, \Delta \mathbf{z}_{51t_1}\}$ were chosen from truncated uniform distributions symmetric about zero. The integrations producing W_2 and W converged with 10^7–10^8 sets of four time-propagations, and showed a robust independence on Metropolis step size. The integrations producing $R^{(3)}$ converged more slowly and with a greater sensitivity to step size. The calculations of $R^{(3)}$ also employed 10^7–10^8 sets of four time propagations. Monte Carlo steps could be rejected either through the Metropolis criterion or if they produced a dissociative trajectory. Dissociative trajectories are generated both from the high-energy tail of the Boltzmann distribution in Eq. (29), and from the phase-space jumps, whose distributions are independent of temperature. All such trajectories were discarded from the calculation, in principle jeopardizing the detailed-balance condition inherent in the Metropolis algorithm. We observed that both the fraction of Monte Carlo moves rejected by the Metropolis criterion f_{rej} and the fraction of dissociative trajectories f_{diss} increased with increasing time. For the parameters $\beta \hbar \omega = 2$ and $\beta D = 25.6$, employed below in Fig. 5, f_{diss} increased to 0.13 and f_{rej} increased from 0.32 to 0.88 during the time ranges studied. For $\beta \hbar \omega = 4$ and $\beta D = 25.6$, the parameters of Fig. 6 below, f_{diss} increased from 0.05 to 0.35, and f_{rej} increased from 0.30 to 0.87. For the parameters used in Fig. 8 below, $\beta \hbar \omega = 5$ and $\beta D = 63.9$, f_{diss} increased from 0.01 to 0.09, and f_{rej} increased from 0.32 to 0.85. This integration procedure has the advantage that the calculation of $R^{(3)}$ is fully parallelizable in the sense that the computations at each set of
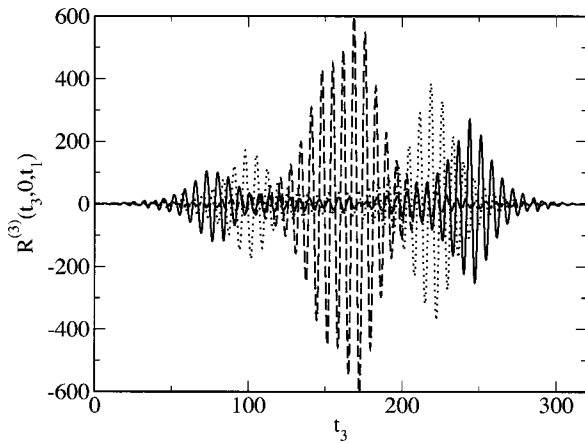
FIG. 1. The third-order response function $R^{(3)}(t_3,0,t_1)$ is calculated from quantum mechanics for $\beta\hbar\omega=0.5$ and $\beta D=25.6$. The delay time is varied from $t_1=75$ (solid curve) to $t_1=100$ (dotted curve) to $t_1=150$ (dashed curve).

time values are performed independently. These semiclassical calculations of $R^{(3)}(t_3,0,t_1)$ are computationally intensive, even for a model of one degree of freedom. Each numerical calculation of $R^{(3)}$ presented in the following section employed approximately 700 sets of values of (t_1,t_3), either ~ 700 values of t_3 for calculations with fixed t_1 or ~ 700 values of both times for calculations with $t_1=t_3$. A typical $R^{(3)}$ calculation required approximately 60 processor days using AMD Athlon MP2000+ processors. This time includes the calculation of W_1 in Eq. (28) (~ 1 processor day), W_2 in Eq. (33) (~ 10 processor days), and W in Eq. (34) (~ 25 processor days), as well as the computation of $R^{(3)}$ in Eq. (18) (~ 25 processor days).

III. NUMERICAL RESULTS

We next present and compare quantum mechanical, classical mechanical, and semiclassical calculations of the third-order response function, $R^{(3)}(t_3,0,t_1)$, for a thermal ensemble of noninteracting Morse oscillators. Quantum mechanical calculations of $R^{(3)}(t_3,0,t_1)$ are shown in Fig. 1 as a function of t_3 for fixed t_1. For the Morse oscillator, the response function in Eq. (2) has the form of the product of a dimensional factor $(m^2\omega D)^{-1}$ and a dimensionless function of ωt_1 and ωt_3 depending on two additional parameters: the classical mechanical quantity βD and the quantum mechanical quantity $\beta\hbar\omega$. Figure 1 and all subsequent figures show the dependence of the dimensionless $m^2\omega D R^{(3)}$ on time variables scaled by ω. In Fig. 1, $\beta D=25.6$ and $\beta\hbar\omega=0.5$. The quantum $R^{(3)}$ is calculated by evaluating Eq. (2) in the energy representation[47] and restricting all sums to bound states. In the limit of impulsive excitation, t_1 corresponds to the delay time between excitation pulses and t_3 is the detection time, typically integrated over in a measurement. The delay time is varied in Fig. 1 from $t_1=75$ in the solid curve to $t_1=100$ in the dotted curve to $t_1=150$ in the dashed curve. For a system characterized by static line broadening, the peak of the echo signal is expected to occur at $t_3\approx t_1$.[41,49] In the present model, the thermal distribution of oscillator energies produces static line broadening, but the pattern of

intensities in the echo signal for an anharmonic oscillator in the absence of dissipation is shown in Fig. 1 to be more complex than that predicted by simpler models of a two-level system.[50]

The response function probed in an echo experiment may be divided into "rephasing" terms with the potential to generate an echo peaked near $t_3\approx t_1$, and "nonrephasing" terms, with the capacity to produce an echo at $t_3\approx -t_1$.[9,22,41,51] A negative value of t_1 corresponds to interchanging the order in time of the two applied pulses.[9,22,41,51] For the Morse oscillator, $R^{(3)}(t_3,0,t_1)$ is nearly periodic both in t_3 and in t_1, with approximate period $\tau\equiv 2\pi/\Delta$, where $\Delta=\hbar\omega^2/2D$ is the anharmonic frequency decrement between successive one-quantum transitions. For fixed t_1, the response function therefore can show a series of echoes at $t_3\approx t_1+n\tau$ and another series of echoes at $t_3\approx -t_1+n\tau$, with n an integer. Figure 1 shows the range $0\leq t_3\leq\tau$, with $\tau\approx 320$. For each t_1 value shown in Fig. 1, the pattern shown repeats nearly periodically over intervals of duration τ. The appearance of $R^{(3)}$ on the interval $0\leq t_3\leq\tau$ depends on the magnitude of t_1 relative both to τ and to $\tau/2$. For $t_1<\tau/2$, there are two significant echoes, unequal in intensity, peaked at $t_3\approx t_1$ and at $t_3\approx\tau-t_1$. The earlier echo arises from the "rephasing" contribution to $R^{(3)}$, while the later echo is a periodic image of the "nonrephasing" contribution peaked at $t_3=-t_1$. This is the situation depicted by the solid and dotted curves in Fig. 1. For $t_1\approx\tau/2$, these two echoes merge into a single peak at $t_3\approx t_1\approx\tau/2$. This is approximately the situation shown by the dashed curve, for which $t_1=150$ and $\tau/2\approx 160$. For $\tau/2<t_1<\tau$, echoes occur at $t_3\approx t_1$ and $t_3\approx\tau-t_1$, but with the "nonrephasing" peak earlier than the "rephasing" one. At $t_1\approx\tau$, the amplitude of the response function is greatly diminished with peaks at $t_3\approx 0$ and $t_3\approx\tau$. These last strongly quantum mechanical cases are not illustrated in Fig. 1. Since $\tau\propto\hbar^{-1}$, in the limit of classical mechanics, $\tau\to\infty$, the period of the echo signal becomes infinite, and the earliest peak of the "nonrephasing" echo for positive t_3 moves towards infinite t_3. The remaining classical echo is peaked at $t_3\approx t_1$.

Quantum and classical mechanical calculations of $R^{(3)}(t_3,0,t_1)$ as a function of t_3 at $t_1=75$ are compared in Fig. 2. The solid curve shows the result of a classical mechanical calculation, computed for $\beta D=25.6$ from the $\hbar\to 0$ limit of Eq. (2),[19,21]

$$R^{(3)}(t_3,0,t_1)=-\frac{\beta}{m}\bigg(\langle[\mathbf{M}_{qp}(\mathbf{z},t_3)]_{00}[\mathbf{M}_{pp}(\mathbf{z},-t_1)]_{00}\rangle$$

$$-\frac{\beta}{m}\langle[\mathbf{M}_{qp}(\mathbf{z},t_3)]_{00}p(-t_1)p(0)\rangle\bigg). \qquad (37)$$

Here, $p(t)$ denotes the momentum of the active degree of freedom, and the angular brackets indicate a thermal average over the canonical phase space distribution. The stability matrices in Eq. (37) are defined in Eq. (7). Trajectories and stability matrices required in Eq. (37) were calculated using the analytical dynamics of the classical Morse oscillator in terms of action-angle variables,[29,47,48] as described in the preceding section. The contribution to the observable from dissociative trajectories is neglected.[29] The dashed curve in Fig.

J. Chem. Phys., Vol. 120, No. 3, 15 January 2004
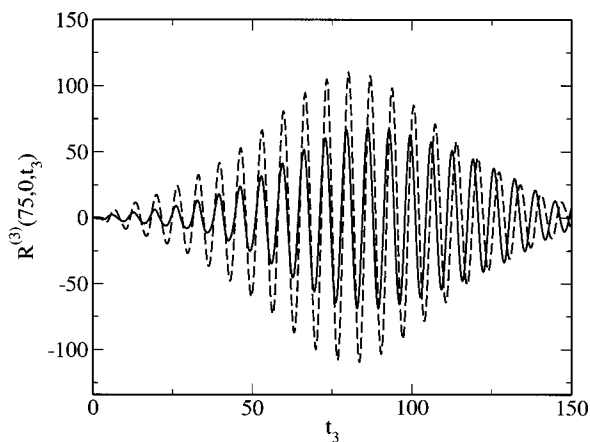
Calculation of the vibrational echo   1497

FIG. 2. The third-order response function $R^{(3)}(t_3,0,t_1)$ is shown for $t_1 = 75$ with $\beta D = 25.6$. The solid curve shows the classical mechanical result from Eq. (37), and the dashed curve shows the quantum result from Eq. (2) with $\beta \hbar \omega = 2.0$.

FIG. 4. The vibrational echo response function $R_E(t)$ is shown for $\beta D = 25.6$. The solid curve is the classical mechanical response, and the dashed curve shows the quantum mechanical result for $\beta \hbar \omega = 2.0$.

2 shows the corresponding quantum mechanical result, also for $\beta D = 25.6$ and with $\beta \hbar \omega = 2.0$, computed from Eq. (2). The approximate period of the quantum response function is $\tau \approx 160$, so that $t_1 = 75 \approx \tau/2$ and the quantum echo displays a single peak on the interval $0 \leqslant t_3 \leqslant \tau$. Classical and quantum echoes are each peaked at $t_3 \approx t_1$ and have similar magnitudes. The rapid oscillation in the quantum case is characterized by a lower frequency than the classical result.

The quantum calculation in Fig. 2 is reproduced as the dashed curve in Fig. 3. The solid curve in Fig. 3 shows the semiclassical calculation from Eq. (15), also for $t_1 = 75$, $\beta D = 25.6$, and $\beta \hbar \omega = 2.0$. The semiclassical result shows excellent agreement with quantum mechanics, both with respect to amplitude and frequency.

Since the echo response is peaked at $t_3 \approx t_1$ in both classical and quantum mechanics, we consider the dependence of the response function near this peak on delay time by defining the echo response function $R_E(t)$ by $R_E(t) \equiv R^{(3)}(t,0,t)$. Calculations of $R_E(t)$ are shown in Fig. 4 for $\beta D = 25.6$. The solid curve shows the classical mechanical result computed from Eq. (37). The classical $R_E(t)$ in Fig. 4 shows an oscillation at a frequency approximately equal to
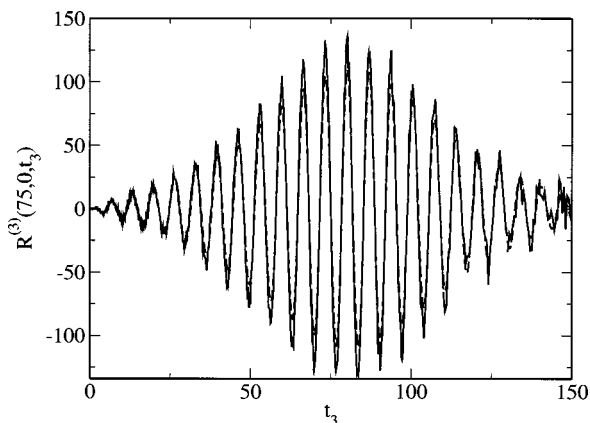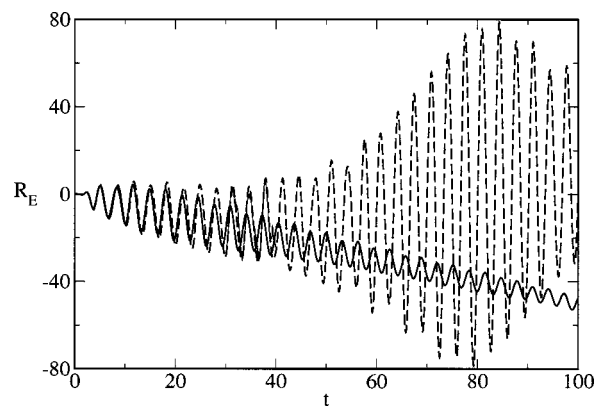
twice the harmonic frequency ω, and a linear drift associated with the linear divergence of stability matrix elements for a one-dimensional anharmonic oscillator.[51–53] The dashed curve in Fig. 4 shows the quantum mechanical $R_E(t)$, also for $\beta D = 25.6$ and with $\beta \hbar \omega = 2.0$, the parameters used in Figs. 2 and 3. Like the classical $R_E(t)$, the quantum mechanical result oscillates at a frequency near 2ω, but with a frequency shift relative to the classical result that is evident in Fig. 4 at longer times. At short times, classical and quantum results agree well, but the envelope of the quantum response function shows a peak near $t_3 = \tau/2 \approx 80$ that is absent in classical mechanics.

The quantum $R_E(t)$ from Fig. 4 is repeated in Fig. 5 as the dashed curve. The solid curve in Fig. 5 shows the semiclassical approximation to R_E, computed from Eq. (15). While the semiclassical approximation slightly overestimates the amplitude, it reproduces the recurrence at $t \approx \tau/2$ and frequency shift that distinguish the quantum from the classical response functions. We next consider the dependence of $R_E(t)$ on $\beta \hbar \omega$ at fixed βD. Since the classical mechanical limit is attained for $\beta \hbar \omega \rightarrow 0$ at fixed βD, increasing $\beta \hbar \omega$ at fixed βD increases the potential importance of quantum effects. The dashed curve in Fig. 6 shows the quantum mechanical R_E for $\beta D = 25.6$ and $\beta \hbar \omega = 4.0$, twice the value of

FIG. 3. The dashed curve repeats the quantum $R^{(3)}(t_3,0,t_1)$ from Fig. 2 for $t_1 = 75$ with $\beta D = 25.6$ and $\beta \hbar \omega = 2.0$, and the solid curve shows the semiclassical result from Eq. (15).
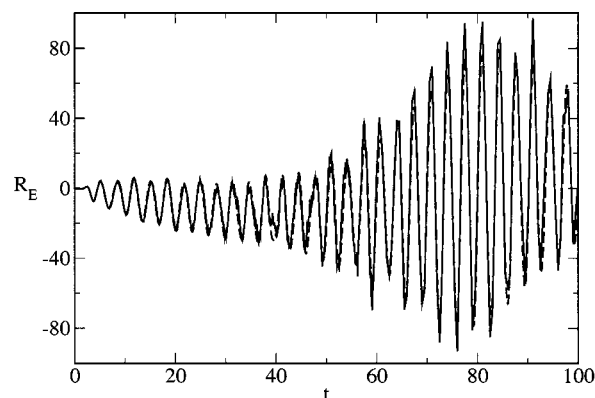

FIG. 5. The vibrational echo response function $R_E(t)$ is shown for $\beta D = 25.6$ and $\beta \hbar \omega = 2.0$. The dashed curve shows the quantum result from Fig. 4, and the solid curve is the semiclassical calculation from Eq. (15).
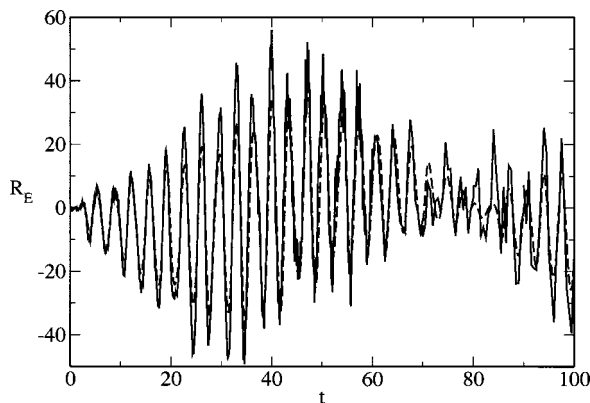
FIG. 6. The vibrational echo response function $R_E(t)$ is shown for $\beta D = 25.6$ and $\beta\hbar\omega = 4.0$. The dashed curve shows the quantum mechanical result, and the solid curve displays the semiclassical calculation from Eq. (15).

$\beta\hbar\omega$ as in Fig. 4. The solid curve shows the semiclassical approximation for $\beta D = 25.6$ and $\beta\hbar\omega = 4.0$, computed from Eq. (15). The accuracy of the semiclassical result degrades, not surprisingly, as $\beta\hbar\omega$ increases. Nevertheless, the semiclassical approximation remains qualitatively correct, reproducing the two dominant frequencies of the quantum result, and even displaying some of the fine structure in the peak amplitudes.

Figures 7 and 8 show the effect on $R_E(t)$ of temperature variation. The quantum (dashed) and classical mechanical (solid) echo response functions are shown in Fig. 7 at a temperature reduced by a factor of 2.5 compared to the cases shown in Fig. 4: $\beta D = 63.9$ and $\beta\hbar\omega = 5.0$. The classical R_E shows the same oscillations and linear drift displayed in Fig. 4, but the amplitude of the oscillations has increased with decreasing temperature. In the quantum mechanical case, the amplitude of oscillations approaching the first recurrence increases more gradually than at higher temperature. The quantum result from Fig. 7 is reproduced as the dashed curve in Fig. 8, while the semiclassical approximation from Eq. (15) is shown by the solid curve. While the semiclassical result overestimates amplitudes somewhat more than at the higher temperature of Fig. 5, the semiclassical approximation re-
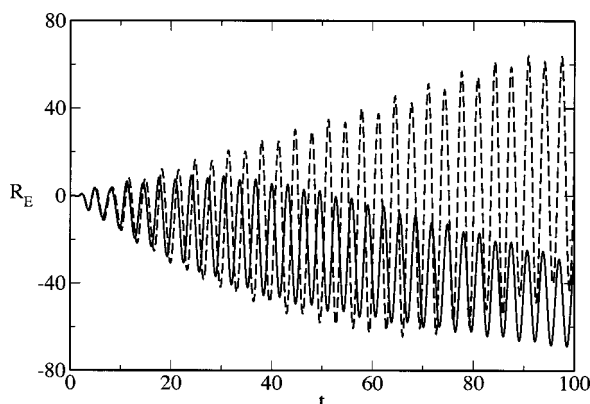

FIG. 7. The vibrational echo response function $R_E(t)$ is shown within classical mechanics at a temperature reduced by a factor of 2.5 compared to Fig. 4, $\beta D = 63.9$, by the solid curve. The quantum result for $\beta D = 63.9$, $\beta\hbar\omega = 5.0$ is shown by the dashed curve.
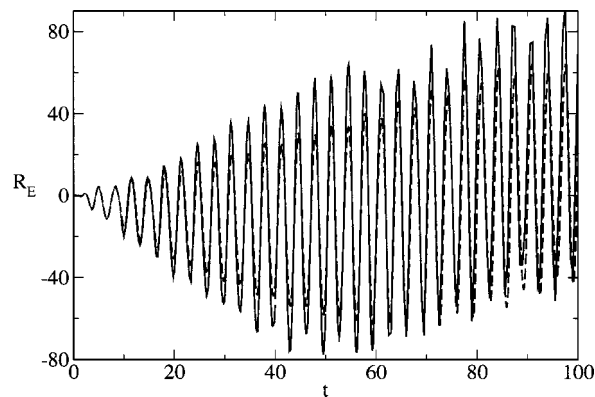

FIG. 8. Quantum (dashed curve) and semiclassical (solid curve) echo response functions are shown for $\beta D = 63.9$, $\beta\hbar\omega = 5.0$, a temperature reduced from that in Fig. 5 by a factor of 2.5.

mains surprisingly accurate at the very low temperature of Fig. 8, despite the use of a high-temperature approximation to the density matrix in Eq. (14).

IV. CONCLUSIONS

Our previous calculations[29] of the linear response function, $R^{(1)}(t)$, for the model of Eq. (35) demonstrated that a semiclassical approximation based on the Herman–Kluk (HK) propagator of Eq. (3) and the high-temperature approximation to the density matrix in Eq. (14) is quantitatively correct over a wide range of temperature. Figures 3, 5, 6, and 8 of the present work demonstrate that this pair of approximations provides an excellent approximation to the quantum mechanical *nonlinear* response function for the same model. For a thermal distribution of noninteracting anharmonic oscillators, the quantum echo response function differs from the classical mechanical limit in exhibiting recurrences and in the existence of a quantum mechanical frequency shift. Both of these effects are reproduced by the semiclassical calculations. These results for a model with a single degree of freedom represent a rigorous test of the semiclassical approach. In a larger system with dissipation, effectively irreversible dephasing processes can obscure the differences between classical and quantum calculations.[22,54] The success of the HK propagator for the vibrational echo calculations reported here suggests that this semiclassical method may be usefully applied to the many measurements in nonlinear vibrational spectroscopy that probe such response functions.[41]

Our findings that the third-order response function relevant to the vibrational echo can be modeled with the HK propagator are consistent with the growing literature[28,33,34] on the successful application of this semiclassical approximation to a variety of dynamical properties. However, previous applications of this propagator to dynamical observables have emphasized *two-time correlation functions*.[32,43,55] An exception is the study of the three-time correlation function related to resonance Raman scattering by Ovchinnikov *et al.*[28] which employed HK dynamics to treat nuclear motions on ground and excited state electronic surfaces. The different physics of this vibronic observable dictated a dif-

ferent mathematical formulation from that employed here to treat an observable involving a single electronic state. The vibronic observable permits the application of the Condon approximation, removing dependence on nuclear coordinates from the dipole operator. As a consequence, the resonance Raman signal could be computed from a single HK "forward-backward" propagator[28,37,56] incorporating dynamics on both electronic surfaces, without the need for repeated propagation steps connected by phase-space jumps. The present work differs in the application of the HK formalism to calculate a *multitime response function* describing nuclear dynamics within a single electronic state. The dependence on nuclear coordinates of the dipole operator must be included, resulting in a semiclassical calculation requiring repeated classical propagation steps, interrupted by phase-space jumps. This work is also distinct from previous semiclassical computations of *correlation functions* in its treatment of a *response function*, a quantum average over commutators of operators, as shown in Eq. (2). By evaluating the commutators explicitly, an nth-order response function could be written as a sum of 2^n correlation functions, each of which could then be evaluated separately. The formalism employed here[29] instead treats the entire response function in a single computation, directly including interference among individual, constituent correlation functions.

Calculation of the echo response function $R_E(t)$ from Eq. (13) for a system of F degrees of freedom requires performing an $8F$-dimensional integral of an integrand whose evaluation requires two pairs of classical trajectories related by a pair of phase-space jumps. Convergence of this calculation for the $F=1$ case treated above required large numbers of classical trajectories per time point, even with the use of an importance sampling algorithm.[43] Calculating R_E by a straightforward application of this approach to large F poses a serious challenge. The calculations presented here demonstrate that a semiclassical method based on the HK propagator can provide accurate calculations of the nonlinear response of an anharmonic system. It remains for the future to develop additional approximations to make the calculation more tractable for large F, while retaining the level of accuracy demonstrated here.

ACKNOWLEDGMENTS

[1] U. Tracht, A. Heuer, and H. Spiess, J. Chem. Phys. **111**, 3720 (1999).
[2] S. Mukamel, A. Piryatinski, and V. Chernyak, Acc. Chem. Res. **32**, 145 (1999).
[3] M. D. Fayer, Annu. Rev. Phys. Chem. **52**, 315 (2001).
[4] P. Hamm and R. M. Hochstrasser, in *Ultrafast Infrared and Raman Spectroscopy*, edited by M. D. Fayer (Dekker, New York, 2001), pp. 273–347.
[5] O. Golonzka, M. Khalil, N. Demirdoven, and A. Tokmakoff, J. Chem. Phys. **115**, 10814 (2001).
[6] J. C. Wright, Int. Rev. Phys. Chem. **21**, 185 (2002).
[7] L. J. Kaufman, J. Y. Heo, L. D. Ziegler, and G. R. Fleming, Phys. Rev. Lett. **88**, 207402 (2002).
[8] M. Khalil, N. Demirdoven, and A. Tokmakoff, J. Phys. Chem. A **107**, 5258 (2003).
[9] P. Hamm, M. Lim, and R. M. Hochstrasser, Phys. Rev. Lett. **81**, 5326 (1998).
[10] J. Stenger, D. Madsen, P. Hamm, E. T. J. Nibbering, and T. Elsaesser, J. Phys. Chem. A **106**, 2341 (2002).
[11] K. A. Merchant, D. E. Thompson, Q.-H. Xu, R. B. Williams, R. F. Loring, and M. D. Fayer, Biophys. J. **82**, 3277 (2002).
[12] K. A. Merchant, W. G. Noid, D. E. Thompson, R. Akiyama, R. F. Loring, and M. D. Fayer, J. Phys. Chem. B **107**, 4 (2003).
[13] K. A. Merchant, W. G. Noid, R. Akiyama, I. J. Finkelstein, A. Goun, B. L. McClain, R. F. Loring, and M. D. Fayer, J. Am. Chem. Soc. **125**, 13804 (2003).
[14] A. Piryatinski and J. L. Skinner, J. Phys. Chem. B **106**, 8055 (2002).
[15] A. Piryatinski, C. P. Lawrence, and J. L. Skinner, J. Chem. Phys. **118**, 9664 (2003).
[16] A. Piryatinski, C. P. Lawrence, and J. L. Skinner, J. Chem. Phys. **118**, 9672 (2003).
[17] S. Mukamel, V. Khidekel, and V. Chernyak, Phys. Rev. E **53**, R1 (1996).
[18] T. Keyes and J. T. Fourkas, J. Chem. Phys. **112**, 287 (2000).
[19] R. B. Williams and R. F. Loring, J. Chem. Phys. **113**, 1932 (2000).
[20] R. B. Williams and R. F. Loring, J. Chem. Phys. **113**, 10651 (2000).
[21] R. B. Williams and R. F. Loring, Chem. Phys. **266**, 167 (2001).
[22] R. Akiyama and R. F. Loring, J. Chem. Phys. **116**, 4655 (2002).
[23] A. Ma and R. M. Stratt, J. Chem. Phys. **116**, 4962 (2002).
[24] S. Saito and I. Ohmine, Phys. Rev. Lett. **88**, 207401 (2002).
[25] C. Dellago and S. Mukamel, Phys. Rev. E **67**, 035205 (2003).
[26] S. Saito and I. Ohmine, J. Chem. Phys. **119**, 9073 (2003).
[27] V. Khidekel, V. Chernyak, and S. Mukamel, in *Femtochemistry: Ultrafast Chemical and Physical Processes in Molecular Systems*, edited by M. Chergui (World Scientific, Singapore, 1996), pp. 507–514.
[28] M. Ovchinnikov, V. A. Apkarian, and G. A. Voth, J. Chem. Phys. **114**, 7130 (2001).
[29] W. G. Noid, G. S. Ezra, and R. F. Loring, J. Chem. Phys. **119**, 1003 (2003).
[30] M. F. Herman and E. Kluk, Chem. Phys. **91**, 27 (1984).
[31] M. F. Herman, Annu. Rev. Phys. Chem. **45**, 83 (1994).
[32] M. F. Herman and D. F. Coker, J. Chem. Phys. **111**, 1801 (1999).
[33] W. H. Miller, Mol. Phys. **100**, 397 (2002).
[34] W. H. Miller, J. Phys. Chem. B **106**, 8132 (2002).
[35] J. Cao and G. A. Voth, J. Chem. Phys. **104**, 273 (1996).
[36] R. Hernandez and G. A. Voth, Chem. Phys. **233**, 243 (1998).
[37] X. Sun and W. H. Miller, J. Chem. Phys. **110**, 6635 (1999).
[38] K. Thompson and N. Makri, Phys. Rev. E **59**, 4729 (1999).
[39] J. Shao and N. Makri, J. Phys. Chem. A **103**, 9479 (1999).
[40] Y. Zhao and N. Makri, Chem. Phys. **280**, 135 (2002).
[41] S. Mukamel, *Principles of Nonlinear Optical Spectroscopy* (Oxford University Press, New York, 1995).
[42] J. R. Klauder and B.-S. Skagerstrom, *Coherent States: Applications in Physics and Mathematical Physics* (World Scientific, Singapore, 1985).
[43] S. X. Sun and W. H. Miller, J. Chem. Phys. **117**, 5522 (2002).
[44] D. Frenkel and B. Smit, *Understanding Molecular Simulation: From Algorithms to Applications* (Academic Press, San Diego, 2002).
[45] P. G. Bolhuis, D. Chandler, C. Dellago, and P. L. Geissler, Annu. Rev. Phys. Chem. **53**, 291 (2002).
[46] K. G. Kay, J. Chem. Phys. **100**, 4432 (1994).
[47] R. B. Shirts, J. Phys. Chem. **91**, 2258 (1987).
[48] M. S. Child, *Semiclassical Mechanics with Molecular Applications* (Oxford University Press, New York, 1991).
[49] G. R. Fleming, Proc. Natl. Acad. Sci. U.S.A. **95**, 15 161 (1998).
[50] J. I. Steinfeld, *Molecules and Radiation: An Introduction to Modern Molecular Spectroscopy* (MIT Press, Cambridge, MA, 1985).
[51] W. G. Noid, G. S. Ezra, and R. F. Loring (unpublished).
[52] J. A. Leegwater and S. Mukamel, J. Chem. Phys. **102**, 2365 (1995).
[53] J. Wu and J. Cao, J. Chem. Phys. **115**, 5381 (2001).
[54] R. Akiyama and R. F. Loring, J. Phys. Chem. A **107**, 8024 (2003).
[55] N. Makri and W. H. Miller, J. Chem. Phys. **116**, 9207 (2002).
[56] O. Kühn and N. Makri, J. Phys. Chem. A **103**, 9487 (1999).